STRUCTURAL AND RADIOMETRIC ASYMMETRY IN BRAIN IMAGES

SARANG JOSHI, PETER LORENZEN, GUIDO GERIG, AND ELIZABETH BULLITT

ABSTRACT. This paper presents a general framework for analyzing structural and radiometric asymmetry in brain images. In a healthy brain, the left and right hemispheres are largely symmetric across the mid-sagittal plane. Brain tumors may belong to one or both of the following categories: mass-effect, in which the diseased tissue displaces healthy tissue; and infiltrating, in which healthy tissue has become diseased. Mass-effect brain tumors cause structural asymmetry by displacing healthy tissue, and may cause radiometric asymmetry in adjacent normal structures due to edema. Infiltrating tumors have a different radiometric response from healthy tissue. Thus, structural and radiometric asymmetries across the mid-sagittal plane in brain images provide important cues that tumors may be present. We have developed a framework that registers images with their reflections across the mid-sagittal plane. The registration process accounts for tissue displacement through large deformation image warping. Radiometric differences are taken into account through an additive intensity field. We present an efficient multi-scale algorithm for the joint estimation of structural and radiometric asymmetry. Results for nine MR images of patients with tumors and four normal control subjects are presented.

Key Words: Brain symmetry analysis, plane of symmetry estimation, deformable image mapping, medical image analysis.

1. INTRODUCTION

The healthy human brain is largely symmetric across the mid-sagittal plane. Recognizing that structural asymmetry may indicate disease, in our previous work we examined shape and volume differences between the left and right hippocampi in patients with schizophrenia [1] [2][3][4], epilepsy [5][6][7], and Alzheimer's disease [8]. Most other work involving structural asymmetry has focused on small-scale geometric

Date: 13 September 2002.

inter-hemispheric differences [9][10][11] [12][13][14][15]. Up to now, little attention has been paid to gross differences between the left and right brain hemispheres in patients with brain tumors. In this paper, an extension of [16], we describe our unified framework for studying not only large- and small-scale structural variations, but also intensity variations occurring in images of patients with brain tumors.

As part of a larger effort aimed at improving the diagnosis and treatment of tumor patients, our group is investigating techniques for analyzing the regional effects and vascular characteristics of brain tumors. The initial stages of this work is aimed toward the automatic identification of tumors in MR images. We are investigating several, potentially synergistic, methods for segmenting tumors: multi-channel (e.g. white matter, grey matter, and cerebrospinal fluid among others) statistical pattern recognition, level set evolution, atlas-based registration, and asymmetry analysis.

Tumors exhibit two main effects in MR images: mass-effect and infiltration. Mass-effect tumors displace and distort the underlying structure. Infiltrating tumors affect the tissue characteristics, changing the radiometric response in images. Most cases show a combination of these two effects. For example, in purely mass-effect tumors, the presence of edema induces changes in the radiometric response of adjacent normal structures. We have developed a single framework to study both structural and radiometric asymmetry in images of patients with brain tumors.

We study the asymmetry of the brain in MR images by registering an image with its reflection about the plane of symmetry. Given a scalar 3D MR image, $I(x) \in \mathbb{R}^+$ where $x = [x_1, x_2, x_3]^T \in \Omega \subset \mathbb{R}^3$, of the brain and corresponding plane of symmetry, the structural deformations and changes in the radiometric response of the tissue due to the the disease process are estimated via the following mean squared error minimization

(1.1)
$$\hat{H},\, \hat{q},\, \hat{d},\, \hat{f} = \arg \min_{H,q,d,f} \int_{\Omega} ||I(x) - I(H(x-q)+q+d(x)) + f(x)||^2 dx$$

where H is a Householder reflection matrix, formally defined in Section 2.1.1, and $q \in \mathbb{R}^3$ is a translation characterizing the plane of symmetry. The high dimensional vector field $d(x) \in \mathbb{R}^3$ describes the geometric deformations in the brain across the plane of symmetry, and the additive scalar intensity field $f(x) \in \mathbb{R}$ describes the intensity variation. The latter two quantities are regularized with derivative operators

to ensure smoothness during the estimation process. Throughout the background of 3D MR image of the brain is assumed to be uniformly black.

In this paper, we present a two-stage algorithm. In the first stage of the process, $\hat{H}$, $\hat{q}$, $\hat{f}$ are estimated through a multi-scale iterative approach while holding the deformation field fixed as the additive identity, $d(x) = 0 \; \forall x \in \Omega$. In this way, we obtain both the estimated plane of symmetry characterized by $\hat{H}$ and $\hat{q}$, and an initial estimate of the intensity variation field, $\hat{f}$.

The second stage estimates the structural deformations characterized by $d(x)$ in Equation (1.1) and refines the estimate of the intensity field variation $f(x)$ via an extension of the large deformation diffeomorphic image warping algorithms developed in [17][18][19].

Section 2 of this paper describes the two-stage process mentioned above. Section 3 presents results of the plane of symmetry estimation and asymmetry analysis of intensity field variation and high dimensional local deformations. The performance of this algorithms is also discussed.

2. Method

The two stage algorithm for estimating structural deformations and intensity variations is depicted in the flow chart show in Figure 2.1 . The remainder of this section details this two-stage process. The following subjection, 2.1, develops the first part of the framework which involves estimating the plane of symmetry and initial intensity field variation. Section 2.2 extends the framework to include high dimensional local deformations.

2.1. **Estimation of Plane of Symmetry.**

Given a scalar 3D MR image, $I(x)$, of the brain we would like to estimate the plane of symmetry as well as investigate the inter-hemispheric asymmetry in the brain. In this paper, we define the plane of symmetry to be the plane about which inter-hemispheric similarity is maximal. This plane is not necessarily the mid-sagittal plane defined by the *anterior commissure* and the *posterior commissure* [20].

A number of techniques have been employed to compute the plane of symmetry in MR images of the brain. Many of these methods involve fitting a 3D plane from a set of symmetry lines extracted from 2D images. Smith and Jenkinson [13] present an algorithm that finds symmetry via symmetry profiles. Of these 2D approaches many employ a cross-correlation symmetry measure. Liu et al. [21][22] extract the plane of symmetry from a set of 2D slices via an edge-based technique.

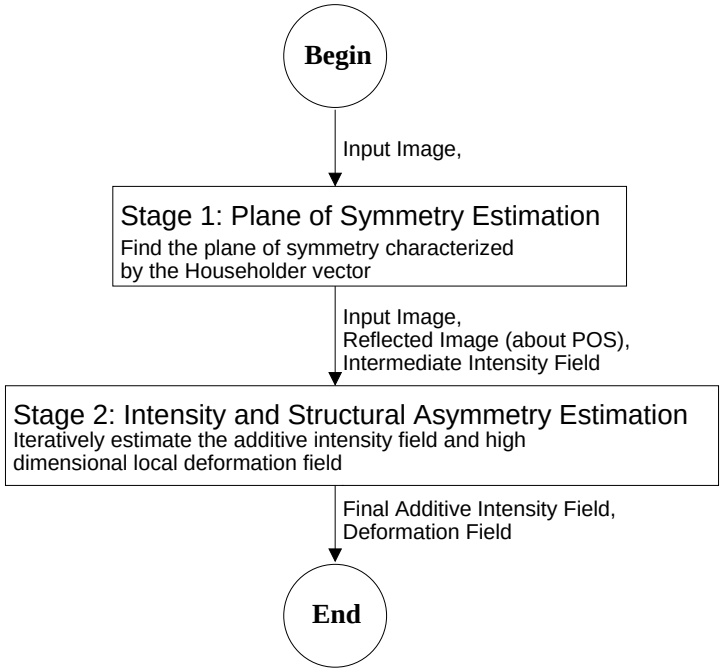

FIGURE 2.1. Flow chart representing the two-stage algorithm

Our approach differs from these methods in that we make a direct estimation of the plane of symmetry from a whole 3D volume. This approach is less sensitive to the variability in the inter-hemispheric fissure. Ardekani [23] et al. present a 3D multi-resolution cross-correlation method for estimating the plane of symmetry. Prima et al [24] present an in-depth analysis of previous plane of symmetry estimation methods along with their own, which involves matching the centers of homologous blocks by reflective symmetry. Rather than performing a series of localized point-to-point correspondences, we estimate the plane of symmetry globally over all Ω. The plane of symmetry is parameterized via the Householder reflection matrix, H, and a translation, q. The inter-hemispheric intensity variation due to the presence of tumors or bias field induced by the MR acquisition or both is modeled as an additive scalar field $f(x)$.

The inter-hemispheric intensity variation due to the presence of tumors is modeled as an additive scalar Gaussian random field, $f(x)$, with covariance induced by a linear differential operator L_f following [25]. Namely, we let $\{f(x),\, x \in \Omega\}$ be a random process process satisfying the stochastic partial differential equation

$$L_f f(x) = e(x) \tag{2.1}$$

where $e(x)$ is white noise. That is, $\langle e, y\rangle \sim N(0, \langle y, y\rangle)$. From [25] we know that $\{f(x),\, x \in \Omega\}$ is a zero-mean Gaussian process with covariance

$$K(x,y) = \int G(x,u)G(y,u)du,$$

where G is the Green's function of L_f satisfying $LG(x,y) = \delta(x-y)$. Since we choose L_f to be the Laplacian, ∇^2, we therefore have $G(x,y) = \frac{1}{||x-y||}$.

Using the Bayesian paradigm the global energy function is defined using a Gaussian mean squared error data likelihood function and the quadratic Gaussian norm induced by the linear differential operator on $f(x)$. The linear differential operator norm enforces smoothness constraints and regularizes the estimation of the the additive intensity field. The optimization, in Equation (1.1), then becomes:

$$\begin{aligned} &\hat{H},\, \hat{q},\, \hat{f} = \\ &\arg\min_{H,q,f} \int_\Omega ||I(x) - I(H(x-q)+q) + f(x))||^2 dx \\ &+\beta \int_\Omega ||L_f f(x)||^2 dx \end{aligned} \tag{2.2}$$

where $L_f = \nabla^2$ is the Laplacian operator.

2.1.1. *Algorithm for Estimating the Plane of Symmetry.* We begin by defining the parameterization of the plane of symmetry via the Householder reflection matrix. We construct a reflection matrix H from a plane characterized by its unit normal vector v shown in Figure 2.2 .

Let p' be the reflection of the point $p \in \Omega$ about the plane of symmetry. We let p_1 be the projection of p onto the line defined by v, that is $p_1 = vv^T p$. Let p_2 be the reflection of p_1 about the origin, $p_2 = -p_1 = -vv^T p$. Therefore, $p' = p + p_2 - p_1$ and, hence, $Hp = Ip - vv^T p - vv^T p = (I - 2vv^T)p$. Thus, given a plane as described by v, we can construct its associated Householder reflection matrix,

$$H = I - 2vv^T, \tag{2.3}$$

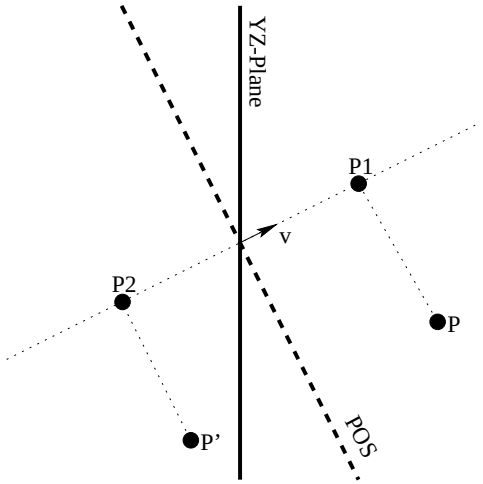

FIGURE 2.2. This figure depicts the Householder reflection construction. The plane of symmetry, POS, is characterized by its normal, v.

where $||v|| = 1$ is the Householder vector. The Householder matrix is symmetric, $H^T = H$, and orthogonal, $H^T H = I$, with determinant $\det |H| = \det |I - 2vv^T| = 1 - 2||v||^2 = -1$.

In our framework an image, $I(x)$, is considered to have perfect symmetry about a plane defined by Householder reflection matrix H passing through point q if

$$\int_\Omega ||I(x) - I(H(x-q)+q)||^2 dx = 0.$$

The iterative algorithm for minimizing the energetics defined in Equation (2.2) is derived by embedding the optimization of the Householder matrix H and corresponding point q in the space of affine motions $GL(3) \times I\!R^3 \subset I\!R^{12}$. Rather than estimating $\hat{H}$ and $\hat{q}$ directly, we estimate an affine matrix, $\hat{A}$, and a translation vector, $\hat{t}$, by a quasi-Newton's method and project the result onto the space of Householder matrices using the Householder projection theorem.

Theorem 1:(Householder Projection Theorem) Let $A \in GL(3)$ be an affine matrix with negative determinant. The Householder reflection matrix, $\hat{H}$, which minimizes the Frobenius norm to A,

$$\hat{H} = \arg\min_H ||A - H||_F, \tag{2.4}$$

is given by:

$$\hat{H} = I - 2ee^T \tag{2.5}$$

where e is the eigenvector associated with the smallest eigenvalue of A.

Proof: From Equations (2.4) and (2.3) we obtain the following relation, which defines $\hat{H}$,

$$\hat{H} = ||A - (I - 2\hat{v}\hat{v}^T)||_F \text{ where} \tag{2.6}$$

$$\hat{v} = \arg\min_v ||A - (I - 2vv^T)||_F. \tag{2.7}$$

where $||\cdot||_F$ denotes the Frobenius norm. Minimizing the right-hand side of Equation (2.7) is equivalent to minimizing the following trace calculation

$$tr[(A-(I-2vv^T))(A-(I-2vv^T))^T] = tr(AA^T)-2tr(A)+4tr(Avv^T)+3.$$

Minimizing the above equation with respect to v reduces to the problem of minimizing $tr(Avv^T)$ with respect to v. Matrix A can be written with its eigen-decomposition, $A = U\Sigma V^T$ where

$$\Sigma = \begin{bmatrix} \sigma_1 & 0 & 0 \\ 0 & \sigma_2 & 0 \\ 0 & 0 & \sigma_3 \end{bmatrix}, \sigma_1 \geq \sigma_2 \geq \sigma_3 \text{ and } V = [e_1\, e_2\, e_3].$$

Construct $v = V\alpha$ for some unit vector $\alpha = [\alpha_1, \alpha_2, \alpha_3]^T$. We then have

$$tr(Avv^T) = tr(U\Sigma V^T V\alpha\alpha^T V^T).$$

Since both U and V^T are orthogonal and thus do not contribute to the trace calculation we simply find a v that minimizes $tr(\Sigma\alpha\alpha^T)$. That is,

$$\begin{aligned} \hat{\alpha} &= \arg\min_\alpha tr(\Sigma\alpha\alpha^T) \\ &= \arg\min_{\alpha_1,\alpha_2,\alpha_3} (\sigma_1\alpha_1^2 + \sigma_2\alpha_2^2 + \sigma_3\alpha_3^2) \\ \text{subject to :} \quad & \alpha_1^2 + \alpha_2^2 + \alpha_3^2 = 1. \end{aligned}$$

This implies that $\hat{\alpha} = [0, 0, 1]^T$. Hence, $v = e_3$ the eigenvector associated with the smallest eigenvalue σ_3 of A.

QED.

With the Householder projection theorem, we embed the optimization in $\mathbb{R}^{12}$ by first registering the image, $I(x)$, with it's reflection, $I_{re}(x)$, about the YZ-plane passing through the image centroid following Prima et al. [10]. Figure 2.3 exemplifies this procedure. In Figure 2.3, $I(x)$ is represented by a solid line depicting an outline of an axial

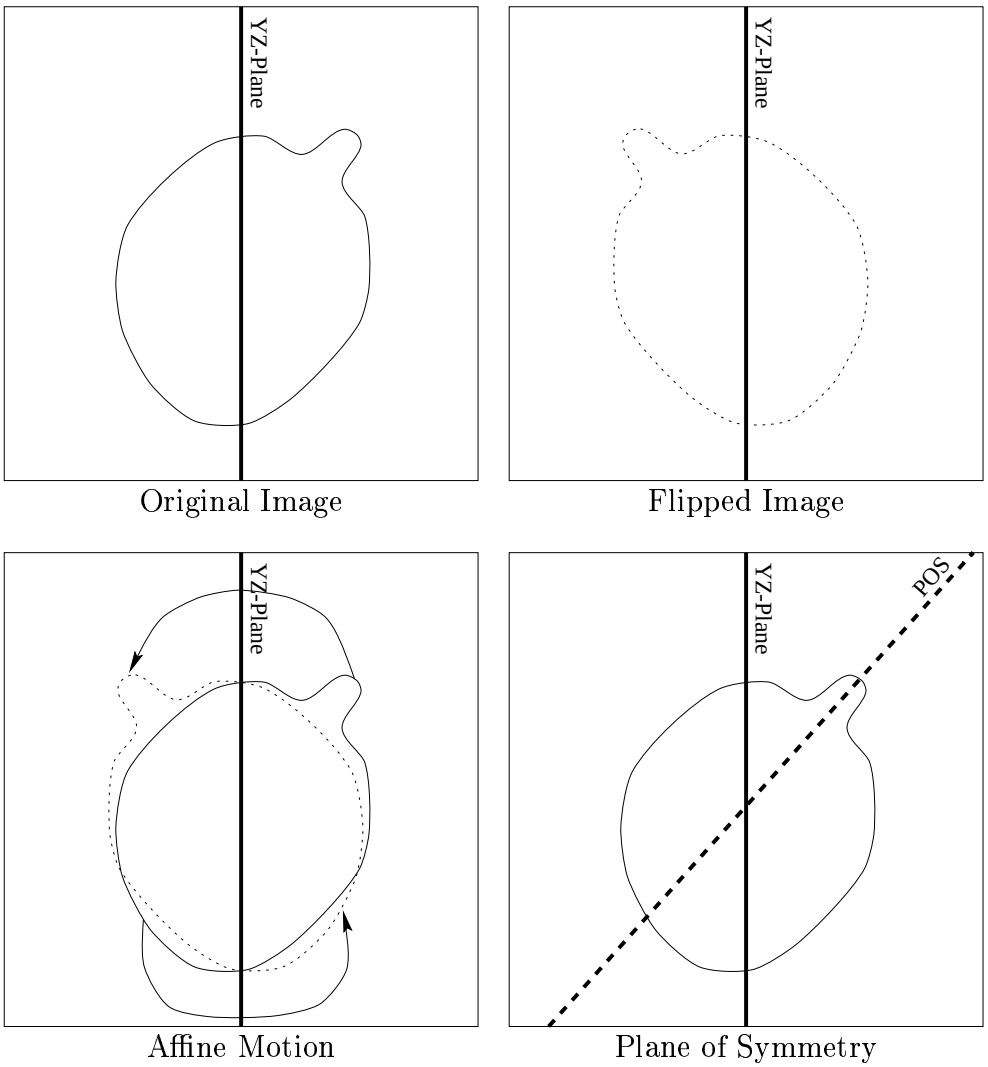

FIGURE 2.3. Reflection Technique
The original image, $I(x)$, is represented as a solid outline in the upper left, the reflected image image, $I_{re}(x)$, as a dotted line in upper right, the affine motion via the arrows in the lower left, and finally, the computed plane of symmetry as the dashed line shown in the lower right.

slice of a skull and $I_{re}(x)$ as a dotted outline. We define the reflected

image, $I_{re}(x)$ via $I_{re}(x) = I(S(x-\mu)+\mu)$ where

$$S = \begin{bmatrix} -1 & 0 & 0 \\ 0 & 1 & 0 \\ 0 & 0 & 1 \end{bmatrix}$$

and μ is the centroid of $I(x)$ calculated from raw intensity values. We estimate the $\hat{A}$, $\hat{t}$, and $\hat{f}$ that minimize the following:

(2.8)

$$\hat{A}, \hat{t}, \hat{f} = \arg\min_{A,t,f} \int_{\Omega} ||I(x) - I_{re}(Ax+t) + f(x)||^2 dx + \beta \int_{\Omega} ||L_f f(x)||^2 dx,$$

where $f(x)$ is the inter-hemispheric intensity variation due to the presence of tumor model as an additive random Gaussian field as described previously.

The lower left panel of the figure illustrates, via the arrows, the estimation of this affine motion, $\hat{A}$ and $\hat{t}$, that takes the original solid line outline into the flipped dotted outline, such that $I_{re}(x) = I(\hat{A}(x-\mu)+\hat{t}+\mu)$. Reflecting $I_{re}(x)$ back across the YZ-plane produces $I(S\hat{A}(x-\mu)+\hat{t}+\mu)$ which best approximates the original image $I(x)$. The estimate of $\hat{H}$ then becomes the projection of $S\hat{A}$, which characterizes the normal, $\hat{v}$, in Equation (2.3) of the plane of symmetry. The estimate $\hat{q}$, which is the point in the point-normal representation of the plane, is given by solving the equation $-\hat{H}\hat{q} + \hat{q} = -\hat{H}\mu + \hat{t} + \mu$. Solving for $\hat{q}$ yields,

$$\begin{aligned} \hat{q} &= \mu + (I - \hat{H})^{-1}\hat{t} \\ &= \mu + \frac{1}{2} v v^T \hat{t}. \end{aligned} \tag{2.9}$$

2.1.2. *Quasi-Newton Optimization Algorithm.* Having parameterized the plane of symmetry via the Householder matrix we now derive the Quasi-Newton optimization algorithm for estimating the affine motion, (A, t). Let $A^k = [a_{ij}^k]$, $t^k = [t_1^k, t_2^k, t_3^k]^T$ be the estimates after iteration k. The iterative algorithm is defined via the update step

$$A^{k+1} = A^k + \Delta A \quad \text{and} \quad t^{k+1} = t^k + \Delta t.$$

We prove that the estimates $(\hat{A}, \hat{t})$ minimizing Equation (2.8) are given by the stable points of the algorithm. For convenience we define the notation,

$$X = \begin{bmatrix} x_1 & x_2 & x_3 & 0 & 0 & 0 & 0 & 0 & 0 & 1 & 0 & 0 \\ 0 & 0 & 0 & x_1 & x_2 & x_3 & 0 & 0 & 0 & 0 & 1 & 0 \\ 0 & 0 & 0 & 0 & 0 & 0 & x_1 & x_2 & x_3 & 0 & 0 & 1 \end{bmatrix}$$

and

$$a^k = \left[\begin{array}{cccccccccccc} a^k_{11} & a^k_{12} & a^k_{13} & a^k_{21} & a^k_{22} & a^k_{23} & a^k_{31} & a^k_{32} & a^k_{33} & t^k_1 & t^k_2 & t^k_3 \end{array} \right]^T.$$

Using the above notation, Equation (2.8) can be written as,

$$E(a^k) = \int_\Omega ||I(x) - I_{re}(Xa^k) + f^k(x)||^2 dx + \beta \int_\Omega ||L_f f^k(x)||^2 dx. \tag{2.10}$$

Let the estimate at iteration $k+1$, a^{k+1}, be given by the update $\Delta a \in \mathbb{R}^{12}$ of a^k, that is

$$a^{k+1} = a^k + \Delta a. \tag{2.11}$$

The energy in Equation (2.10) at iteration $k+1$ then becomes,

$$E(a^{k+1}) = \int_\Omega ||I(x) - I_{re}(X(a^k + \Delta a)) + f^k(x)||^2 dx + \beta \int_\Omega ||L_f \cdot f^k(x)||^2 dx.$$

Using the Taylor series expansion of $I_{re}(x)$ up to the second order about Xa^k, we approximate E^{k+1} as follows,

$$E(a^{k+1}) \approx \int_\Omega ||I(x) - [I_{re}(x) - \nabla I_{re}\,|^T_{Xa^k}\,(X\Delta a)] + f^k(x)||^2 dx + \beta \int_\Omega ||L_f f^k(x)||^2 dx \tag{2.12}$$

Notice that Equation (2.12) is quadratic with respect to Δa. The update step Δa is chosen to minimize $E(a^{k+1})$ which implies

$$\nabla_{\Delta a} E = 0.$$

Applying this gradient we obtain,

$$\nabla_{\Delta a} E = \int_\Omega [I(x) - I_{re}(Xa^k) + f^k(x)] V(x)^T dx + \left(\int_\Omega V(x)^T V(x) dx \right) \Delta a = 0$$

where $V(x) = \nabla I_{re}|^T_{Xa^k} X$. Thus,

$$\Delta a = - \left[\int_\Omega V(x)^T V(x) dx \right]^{-1} \int_\Omega [I(x) - I_{re}(Xa^k) + f^k(x)] V(x)^T dx \tag{2.13}$$

Theorem 2: The stable points $\hat{a} = (\hat{A}, \hat{t})$ of the above iterative algorithm minimize the energy in Equation (2.8) and satisfy the necessary condition

$$\nabla_a E(\hat{a}) = 0.$$

Proof: If $\hat{a}$ is a stable point of the above algorithm then the update Δa in Equation (2.13) is zero implying that

$$\int_\Omega [I(x) - I_{re}(Xa^k) + f^k(x)]V(x)^T dx = 0,$$

where, as before, $V(x) = \nabla I_{re}|^T_{Xa^k} X$. This is exactly the necessary condition for minimizer $\nabla_a E(\hat{a}) = 0$.

QED.

After convergence of the algorithm we compute the estimate for the Householder reflection. From the Householder Projection Theorem and Equation (2.9) we have $\hat{H} = I - 2ee^T$ where e is the eigenvector associated with the smallest eigenvalue of $S\hat{A}$ and $\hat{q} = \mu + \frac{1}{2}ee^T\hat{t}$.

2.1.3. *Intensity Field Estimation.* At each iteration of the Quasi Newton algorithm derived above for estimating (A, t), an estimate for the inter-hemispheric intensity variation $f^k(x)$ is obtained by minimizing

(2.14)
$$f^k = \arg\min_f E(f) = \int_\Omega ||I(x) - I_{re}(A^k x + t^k) + f(x)||^2 dx + \beta \int_\Omega ||L_f f(x)||^2 dx,$$

where A^k, t^k are the estimates of the affine motion and $f^k(x)$ is the intensity field variation estimate at the k^{th} iteration. The necessary condition for the minimizer of (2.14) is that the Gateaux differential $\delta E(f;\eta)$ for all allowable perturbations η is zero [26]

$$\begin{aligned}
\delta E(f:\eta) &= \frac{d}{d\alpha}[\int_\Omega ||I(x) - I_{re}(A^k x + t^k) + f^k(x) + \alpha\eta(x)||^2 dx \\
&\quad + \beta \int_\Omega ||L_f(f^k(x) + \alpha\eta(x))||^2 dx]|_{\alpha=0} dx \\
&= \int_\Omega 2[I(x) - I_{re}(A^k x + t^k) + f^k(x) + \alpha\eta(x)]\eta(x)|_{\alpha=0} dx \\
&\quad + \beta \int_\Omega 2L_f L_f^\dagger (f^k(x) + \alpha\eta(x))\eta(x)|_{\alpha=0} dx \\
&= 2[\int_\Omega [I(x) - I_{re}(A^k x + t^k) + f^k(x)]\eta(x) dx \\
&\quad + \beta \int_\Omega L_f L_f^\dagger f^k(x) dx]\eta(x) dx
\end{aligned}$$

where $L_f^\dagger$ is the adjoint of L_f. The conditions $\delta E(f;\eta) = 0$ for all $\eta(x)$ imply that $f^k(x)$ satisfy the differential equation,

$$I(x) - I_{re}(A^k x + t^k) + f(x) + \beta L_f L_f^\dagger f(x) = 0. \tag{2.15}$$

The above differential equation is solved using the Fast Fourier Transform as follows. Let Ω be a periodic discrete lattice having dimensions $L \times M \times N$. Further define the residue at iteration k to be $r^k(x) = [I_{re}(A^k x + t^k) - I(x)]$. Given this, the intensity differential equation (2.15) can be re-stated as,

$$[\beta L_f^+ L_f + 1] f^k(x) = r^k(x). \tag{2.16}$$

We write $f^k(x)$ and $r^k(x)$ in terms of their Fourier representations,

$$f^k(x) = \sum_{w=0}^{N-1} \sum_{v=0}^{M-1} \sum_{u=0}^{L-1} F^k(u,v,w) e^{j<\omega,x>}$$
$$r^k(x) = \sum_{w=0}^{N-1} \sum_{v=0}^{M-1} \sum_{u=0}^{L-1} R^k(u,v,w) e^{j<\omega,x>}$$

where $\omega = [\omega_u, \omega_v, \omega_w]^T$ with $\omega_u = \frac{2\pi u}{L}, \omega_v = \frac{2\pi v}{M}, \omega_w = \frac{2\pi w}{N}$ and F^k, $R^k \in \mathbb{C}$. We re-write Equation (2.16) as,

$$L f^k(x) = \sum_{w=0}^{N-1} \sum_{v=0}^{M-1} \sum_{u=0}^{L-1} L e^{j<\omega,x>} F^k(u,v,w) \tag{2.17}$$

where $L = \beta L_f L_f^\dagger + 1$. As L is a differential operator with complex exponentials as it's eigenfunctions. Equation (2.17) becomes

$$L f^k(x) = \sum_{w=0}^{N-1} \sum_{v=0}^{M-1} \sum_{u=0}^{L-1} \lambda(u,v,w) e^{j<\omega,x>} F^k(u,v,w),$$

where $\lambda(u,v,w)$ are the eigenvalues of the operator L. We now compute the eigenvalues $\lambda(u,v,w)$:

$$\begin{aligned} \lambda(u,v,w) e^{j<\omega,x>} &= L e^{j<\omega,x>} \\ &= (\beta L_f L_f^\dagger + 1) e^{j<\omega,x>} \\ &= (\beta \lambda_f^2(u,v,w) + 1) e^{j<\omega,x>} \end{aligned} \tag{2.18}$$

where $\lambda_f(u,v,w)$ are the eigenvalues of the operator $L_f = \nabla^2$. Using the standard definition of the finite differences approximation of the Laplacian,

$$\begin{aligned}\nabla^2 e^{j(\omega_u x_1+\omega_v x_2+\omega_w x_3)} \approx \quad & e^{j\omega_u(x_1+1)} + e^{i\omega_u(x_1-1)} - 2e^{j\omega_u x_1} \\ + \quad & e^{j\omega_v(x_2+1)} + e^{i\omega_v(x_2-1)} - 2e^{j\omega_v x_2} \\ + \quad & e^{j\omega_w(x_3+1)} + e^{i\omega_w(x_3-1)} - 2e^{j\omega_w x_3},\end{aligned}$$

the eigenvalues become,

$$\lambda_f(u,v,w) = 2\cos\omega_u + 2\cos\omega_v + 2\cos\omega_w - 6. \tag{2.19}$$

Substituting (2.19) into (2.18) we obtain,

$$\begin{aligned}\lambda(u,v,w) = \quad & 4\beta[-6(\cos\omega_u + \cos\omega_v + \cos\omega_w) \\ & +2(\cos\omega_u\cos\omega_v + \cos\omega_u\cos\omega_w + \cos\omega_v\cos\omega_w) \\ & +\cos^2\omega_u + \cos^2\omega_v + \cos^2\omega_w + 9] + 1.\end{aligned}$$

Finally, we can compute $f(x)$ by taking the inverse Fast Fourier Transform,

$$f^{k+1}(x) = \frac{1}{2\pi LMN}\sum_{w=0}^{N-1}\sum_{v=0}^{M-1}\sum_{u=0}^{L-1}\frac{1}{\lambda(u,v,w)}R^k(u,v,w)e^{-j<\omega,x>}.$$

2.1.4. *Multi-scale Approach to Estimating the Affine Motion.* For an efficient implementation we employ a multi-scale approach in estimating $\hat{A}$ and $\hat{t}$ directly from $I(x)$. We construct a pyramid of three images of decreasing size taken at increasing scale via Gaussian kernel convolutions, $I(x;\sigma) = G(0,\sigma)\bigotimes I(x)$ where $\sigma = 2\tau$ and $\tau = 2$, 4, 8 voxels. The estimation process begins with the images at the largest scale by estimating $\hat{A}$ and $\hat{t}$ for the image. The results of this process become the initialization for the estimation process for the next smaller scale image. This process is repeated until $\hat{A}$ and $\hat{t}$ are estimated at the original scale of $I(x)$.

The convergence criteria for progress to successive scales is simply that both $||A^{k+1} - A^k|| < \varepsilon$ and $||t^{k+1} - t^k|| < \varepsilon$ for some sufficiently small ε.

An initial estimate for A^0 and t^0 is obtained via the method of moments as follows: assuming that the image, $I(x)$, has finite first and second moments, the first and the second moments of the image $I(x)$

become

$$\begin{aligned} \mu_I &= \frac{1}{\int_\Omega I(x)dx}\int_\Omega xI(x)dx \\ K_I &= \frac{1}{\int_\Omega I(x)dx}\int_\Omega (x-\mu_I)(x-\mu_I)^T I(x)dx \end{aligned}$$

If A is a general non-singular affine matrix the first and second moments of the image, $\tilde{I}(x) = I(Ax+t)$, can be expressed as

$$\begin{aligned} \mu_{\tilde{I}} &= \mu_I - t \\ K_{\tilde{I}} &= AK_IA^{-1} \end{aligned} \tag{2.20}$$

Let $S_1 = \sqrt{K_I}$ and $S_2 = \sqrt{K_{\tilde{I}}}$. From Equations (2.20) it follows that $A = S_1S_2^{-1}$ and $t = \mu_I - \mu_{\tilde{I}}$. Using this construction the initial estimates A^0 and t^0 are computed by calculating the first and second moments of the image $I(x)$ and it's reflected image $I_{re}(x)$.

2.2. **Analysis of Inter-hemispheric Geometric Deformations via Image Mapping .** After estimating the plane of symmetry, attention now focuses on small scale geometric differences across the plane of symmetry. The approach developed is similar to the work of Thirion et al. in that the geometric variation is captured via the definition of a high dimensional deformation field. However in previous work [27][28], such analyses have been directed purely toward detection of geometric differences. We present an algorithm that jointly estimates deformation and inter-hemispheric radiometric intensity differences. The method used for estimating the deformation field is an extension of the fluid flow formulation of Christensen et al. and is only briefly described here. For a complete description of the deformation algorithm see [17][18][19].

The high dimensional displacement vector field $d(x)$ and the scalar intensity field $f(x)$ are estimated using an alternating optimization technique that minimizes the quadratic error

$$E = \int_\Omega ||I(x) - I_{re}(H(x-q)+q+d(x)) + f(x)||^2 dx + \beta \int_\Omega ||L_f f(x)||^2 dx$$

where the $L_f = \nabla^2$ is a Laplacian operator that ensures smoothness of the estimate of $f(x)$ as in Equation 2.2 in the plane of symmetry estimation. The regularization parameter β controls the influence of inter-hemispheric intensity variation on the estimation of the displacement field, $d(x)$. As $\beta \to 0$, no regularization penalty is incurred on the

intensity field $f(x)$ and, hence, results in the trivial solution become,

$$\begin{aligned} d(x) &= 0 \\ f(x) &= I_{re}(H(x-q)+q) - I(x). \end{aligned}$$

As $\beta \to \infty$, the inter-hemispheric intensity variation is accommodated entirely by the displacement field, $d(x)$. In this paper we do not study the optimal choice of regularization parameters.

Following Christensen, the deformation field $d(x)$ is defined via an integration of an O.D.E.

$$d(x) = x + \int_0^1 v(d(x,t),t)dt.$$

Energetics are induced on the velocity field $v(\cdot,t)$ using the Navier-Stokes operator $L_d = a\nabla^2 + b\nabla\cdot\nabla + cI$. The energetics induced on the velocity field become

$$E(v) = \int_0^1 \int_\Omega ||L_d v(x,t)||^2 dxdt.$$

Following [18], a computationally efficient algorithm for image matching is used which exploits the fact that the Navier-Stokes operator does not differentiate in time. A time indexed, $t_k, k = 1, \cdots, N$, sequence of optimizations are solved for a locally optimum velocity field $v(x,t_k)$. The transformation is then computed by forward integrating the locally optimum velocity field

$$d(x,t_{k+1}) = d(x,t_k) + \int_{t_k}^{t_{k+1}} v(d(x,\sigma),\sigma)d\sigma.$$

Since this is a locally-in-time optimal method the dimensionality of the optimization is reduced. The radiometric intensity variation is incorporated into this framework by performing the optimization for $f(x)$ at each time step

$$\begin{aligned} f^k(x) &= \arg\min_f \int_\Omega ||I(x) - (I_{re}(H(x-q)+q+d(x,t_k)) + f(x)||^2 dx \\ &\quad +\beta \int_\Omega ||L_f f(x)||^2 dx. \end{aligned}$$

The above optimization is computed using the Fast Fourier Transform as described in section 2.1.3.

In analyzing the computed displacement, $d(x)$, we examine two derived properties of the deformation field: the Jacobian and divergence. We are not the first to use these properties to study volumetric changes in structures within the brain for pathology detection. P. Thompson

and A. Toga use local vector field operations to construct tensor maps that describe magnitude and principal directions of tissue dilation and contraction as well as local rates of change in dynamically changing brains [29]. J. P. Thiron and G. Calmon use local vector field operators to analyze deformations to detect and quantify multiple-sclerosis lesions in the brain [30].

2.2.1. *The Jacobian.* In studying the inter-hemispheric geometric differences we first consider volumetric change due to the deformation field, $d(x)$. Given a linear transformation $T : \mathbb{R}^3 \rightarrow \mathbb{R}^3$ the volume of an object S under that transformation is

$$\text{volume of } T(S) = |\det T| \times \text{volume of } S. \tag{2.21}$$

In our case, T is defined as the Jacobi matrix of the transformation $h(x) = x + d(x)$ with respect to x,

$$T = \frac{\partial h}{\partial(x_1, x_2, x_3)}.$$

Hence, the change in volume, as a scale, is measure by the Jacobian of T, defined as the absolute value of the determinant of Jacobi matrix T:

$$J(T) = |\det T| \tag{2.22}$$

$$= \left|\det\left(I + \frac{\partial(d_1, d_2, d_3)}{\partial(x_1, x_2, x_3)}\right)\right|. \tag{2.23}$$

The Jacobian of T, and hence of $h(x)$, captures the local inter-hemispheric volume differences of corresponding anatomical structures.

This scaling of volume can be thus interpreted in the following manner:

$$J(T) \begin{cases} < 1 & \text{contraction of volume} \\ = 1 & \text{no change in volume} \\ > 1 & \text{dilation of volume} \end{cases}$$

Correspondingly, $\log J(T) < 0$, $\log J(T) = 0$, and $\log J(T) > 0$ indicate contraction, no change, and dilation of volume respectively.

Shown in Figure 2.4 are a grid, x, the grid under a hypothetical deformation characterized by a contraction (upper left) and a dilation (lower right), $h(x)$, along with the logarithm of the Jacobian, $\log J(T)$. The latter is rendered using a spectral colormap where negative values are indicated by violet and blue hues, zero as medium green, and positive values as yellow, orange and red. Notice that the contraction in

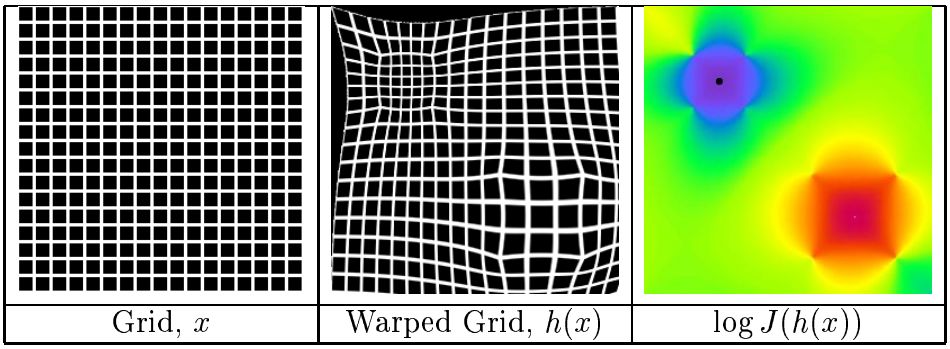

FIGURE 2.4. Determinant of Jacobian Example

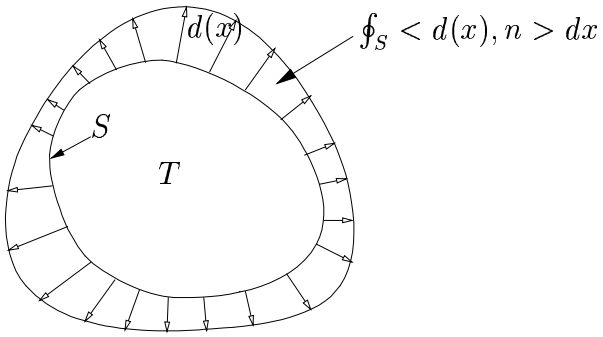

FIGURE 2.5. Divergence

the upper left appears as a blue and violet region in the logarithm of Jacobian image and that the dilation is indicated by orange and red.

2.2.2. *Divergence.* Another measure of volume change is motivated by the use of the Divergence Theorem where we capture local inter-hemispheric shape variation using the divergence operator [31]. For any closed surface S bounding a regular region T, the surface integral $\oint_S \langle d(x), n \rangle ds$ captures the total change of the surface in its normal direction as show in Figure 2.5 . By the Divergence Theorem, this change is given by the integral of the divergence,

$$\oint_S \langle d(x), n \rangle ds = \int_T \nabla \cdot d(x) dx,$$

where T is a regular region, an open set that is equal to the interior of its closure, bounded by a surface S and n is the local surface normal to S. In this figure, the change in the surface is depicted by the movement of the solid via the normals which are represented by arrows. The value of the integration is indicated in the figure.

The divergence of a vector field can also be viewed as the trace of the Jacobian matrix. In the case of the aforementioned transformation, $h(x)$, this is

$$\begin{aligned} \operatorname{div} h(x) &= \operatorname{tr} \frac{\partial(h_1, h_2, h_3)}{\partial(x_1, x_2, x_3)} \\ &= \sum_{i=1}^{3} \frac{\partial h_i}{\partial x_i}. \end{aligned} \tag{2.24}$$

3. Results

Results are presented for the mid-plane estimation in Sub-section 3.1, followed by results obtained for the intensity variation and structural deformation in Sub-section 3.2. These results are based on the study of nine MR images of tumor bearing patients and four MR images of health normal controls.

The nine tumor patient, T1-weighted, images were acquired using a 1.5 Telsa Siemens Magnetome Vision MR scanner. Four of these images are $256 \times 256 \times 130$ in size with spatial resolution 0.8984mm $\times$ 0.8984mm $\times$ 1.5mm. Three of these images are $256 \times 256 \times 120$ in size with spatial resolution 0.9375mm $\times$ 0.9375mm $\times$ 1.5mm. The remaining two images are $256 \times 256 \times 52$ in size with spatial resolution 0.8984mm $\times$ 0.8984mm $\times$ 3.0mm.

The four normal control gradient-echo T1-weighted images were acquired using a 1.5 Telsa GE Signa Scanner. These $256 \times 256 \times 128$ images have spatial resolution 0.9375mm $\times$ 0.9375mm $\times$ 1.5mm.

3.1. Plane of Symmetry Estimation.

We have analyzed the performance of the plane of symmetry estimation algorithm on nine tumor patients. We have found that the plane of symmetry estimation algorithm to be visually robust in the presence of large tumors as well as to the original alignment of the plane of symmetry with respect to the YZ-plane. Figure 3.1 presents two sets of axial and coronal slices of images of patients with tumors. The estimated plane of symmetry is shown in magenta. Figure 3.2 provides a validation test image of a patient which has been rotated axially twenty degrees. The image on the left shows the estimated plane of symmetry through an axial slice of data. The right side images shows a 3D iso-surface rendering of the same image with the estimated 3D plane of symmetry. Notice that the estimation of the plane of symmetry, also shown in magenta, is robust in the presence of the tumor.

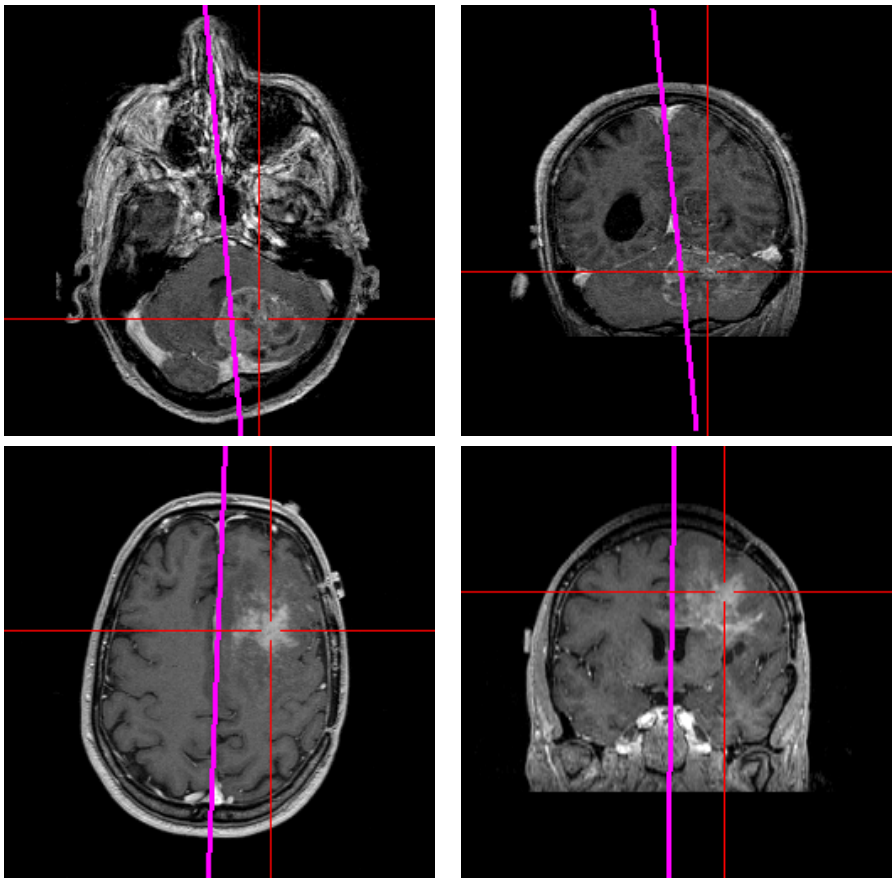

FIGURE 3.1. Two sets of axial and coronal slices of MR images of patients with tumors. The estimated plane of symmetry is shown as magenta line.

To validate the plane of symmetry estimation we computed the plane of the symmetry for each of the nine tumor patient images and four normal control images for known rotations of the images by 0, 5, 10, 15, 20, and 25 degrees axially. The angle between the computed Householder vector of each rotated image and the computed Householder vector of the non-rotated image is produced. The results of this computation are presented in Table 1 and Table 2. Since the algorithm for computing the Householder vector, described in Section 2.1.1, estimates an affine motion of an image through its reflection across the YZ-plane, the rotation captured by the affine estimation is twice that of the computed Householder vector. That is, the known rotations for the affine motion are 0, 10, 20, 30, 40, and 50 degrees axially.

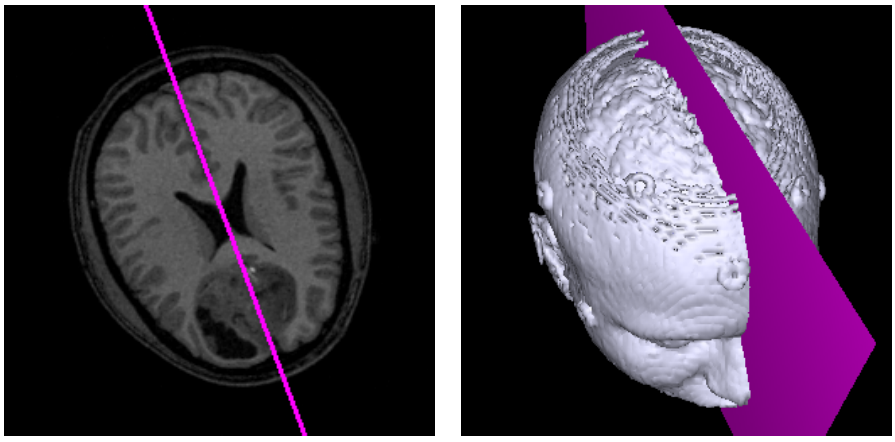

20 Degree Axial Rotation 3D Iso-surface

FIGURE 3.2. Shown on the left is an axial slice through the patient with the estimated plane of symmetry shown in purple. The right panel shows the 3D rendering of the skin as well as the estimated plane of symmetry. Notice the robustness of the algorithm in the presence of the large tumor.

TABLE 1. Computed Householder Angles for Normal Controls

Rotation	5^o	10^o	15^o	20^o	25^o
	4.9807	9.9897	14.9916	19.9946	24.9893
	4.9981	10.0178	15.0220	20.0271	25.0247
	5.0078	10.0145	15.0255	20.0342	25.0303
	4.9988	10.0076	15.0143	20.0216	15.0206
Average Error	0.0075	0.0126	0.0175	0.0221	0.0216

Computed angles between the Householder vector of the non-rotated image, v_0, and that of the Householder vector of each rotated image, v_r: $\theta = \arccos(\langle v_0, v_r \rangle)$.

From the results it can be seen that for the normal subjects the algorithm is robust for angles up to 25 degrees. For all but two of the tumor subjects the method estimates the 25-degree rotation to within 0.1902 degrees. Given the typical placement of the subjects in MR scanners, we do not expect rotations of more than 15 degrees.

Figures 3.3 and 3.4 show plane of symmetry estimation and simple reflection difference image respectively for an image of a normal control subject.

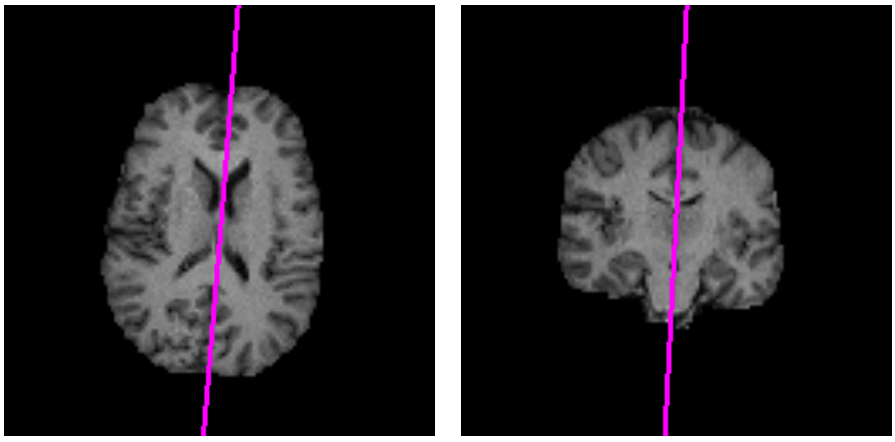

Axial Coronal

FIGURE 3.3. Plane of symmetry estimation results for a given control subject.

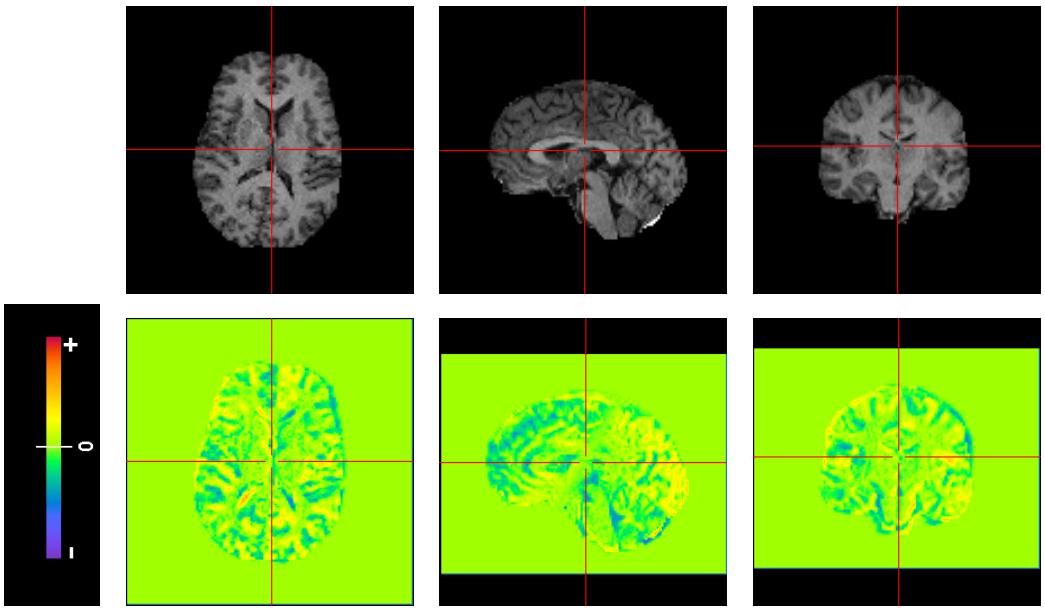

Axial Sagittal Coronal

FIGURE 3.4. The top row of the figure shows the axial sagittal and the coronal views through an example control image . The bottom row shows the difference between the original and reflected images, where blue and violet represent negative values, yellow and red represent positive values, and green represents values near zero.

TABLE 2. Computed Householder Angles for Tumor Patients

Rotation	5^o	10^o	15^o	20^o	25^o
	5.0302	10.0476	15.0642	20.0728	20.2522
	4.9631	9.9801	14.9912	19.9993	25.0123
	4.9091	9.9129	14.9114	19.9005	24.0192
	4.9776	9.9802	14.9833	19.9812	24.9662
	5.0010	9.9979	14.9998	19.9942	24.9822
	4.9377	9.9517	14.9593	19.9344	24.8775
	4.9440	9.9231	14.9078	19.8912	24.8878
	4.9566	9.9603	14.9697	19.9600	24.9480
	4.9978	9.9889	14.9803	19.9688	17.5397
Average Error	0.0384	0.0392	0.0402	0.0492	1.5044

Computed angles between the Householder vector of the non-rotated image, v_0, and that of the Householder vector of each rotated image, v_r: $\theta = \arccos(\langle v_0, v_r \rangle)$.

3.2. **Asymmetry: Tumor Subjects and Normal Controls.** We have applied the algorithms presented in Section 2 for the study of brain asymmetry in images of the nine tumor patients. The top row of Figure 3.5 shows the axial, sagittal, and coronal views of a patient with a right frontal glioma. The plane of symmetry estimation algorithm, 3.1, was used to produce the reflected image across the plane of symmetry shown in the bottom row. The high dimensional deformation vector field, $d(x)$, capturing the normal and pathological inter-hemispheric geometric variability and the intensity field, $f(x)$, capturing the radiometric variation were calculated using the algorithm described in 3.2. Figure 3.6 indicates the computed deformation and shows tumor as the bright region in right frontal region of the brain. More strikingly the tumor is evident as the dark purple region present in the computed intensity field image show in Figure 3.7 .

For the normal control image shown in Figure 3.4 computed Jacobian and Divergence results are presented in Figure 3.8 . The corresponding computed additive intensity field is shown in Figure . As would be expected from normal healthy subjects, from these two figures there is no discernible asymmetry.

For the purposes of comparison we examined the per-voxel average displacement norm, $||d(x)||^2$, and additive intensity field norm, $||f(x)||^2$ normalized with respect to brain volumes for all the images. The results of which are presented in Tables 3 and 4 for the tumor and control group respectively. In addition, per-voxel average regularization norms are presented in Tables 5 and 6 . From these results one can see, in

TABLE 3. Per-voxel Average Tumor Subject Norms

Brain Volume (cm^3)	$\frac{1}{N}\int_\Omega \|\|d(x)\|\|^2 dx$	$\frac{1}{N}\int_\Omega \|\|f_{\text{final}}(x)\|\|^2 dx$
1,641.5	0.2706	2.1412
1,306.0	0.2468	1.7841
1,582.4	0.3213	1.0743
1,345.5	0.2026	1.2944
1,363.5	0.2994	1.4087
1,363.1	0.3755	0.9969
1,388.3	0.9872	4.5946
1,299.2	0.3109	0.2737
1,618.1	0.3361	1.3816

$d(x)$ is measured in voxel space
$f(x)$ is measured in intensity units
N is the number of voxels in the brain volume

TABLE 4. Per-voxel Average Normal Control Norms

Brain Volume (cm^3)	$\frac{1}{N}\int_\Omega \|\|d(x)\|\|^2 dx$	$\frac{1}{N}\int_\Omega \|\|f_{\text{final}}(x)\|\|^2 dx$
1,335.0	0.4099	0.4704
1,395.3	0.2944	0.8456
1,344.3	0.5310	0.9584
1,680.6	0.3256	0.5896

$d(x)$ is measured in voxel space
$f(x)$ is measured in intensity units
N is the number of voxels in the brain volume

TABLE 5. Per-voxel Average Tumor Subject Regularization Norms

Brain Volume (cm^3)	$\frac{1}{N}\int_\Omega \|\|L_d d(x)\|\|^2 dx$	$\frac{1}{N}\int_\Omega \|\|L_f f_{\text{final}}(x)\|\|^2 dx$
1,641.5	9.029e-04	6.83e+03
1,306.0	7.054e-04	4.69e+03
1,582.4	1.710e-03	7.97e+03
1,345.5	1.004e-03	1.15e+04
1,363.5	1.208e-03	7.84e+03
1,363.1	1.261e-03	7.45e+03
1,388.3	2.719e-03	1.21e+04
1,299.2	1.380e-03	2.57e+03
1,618.1	1.264e-03	9.60e+03

$d(x)$ is measured in voxel space
$f(x)$ is measured in intensity units
N is the number of voxels in the brain volume

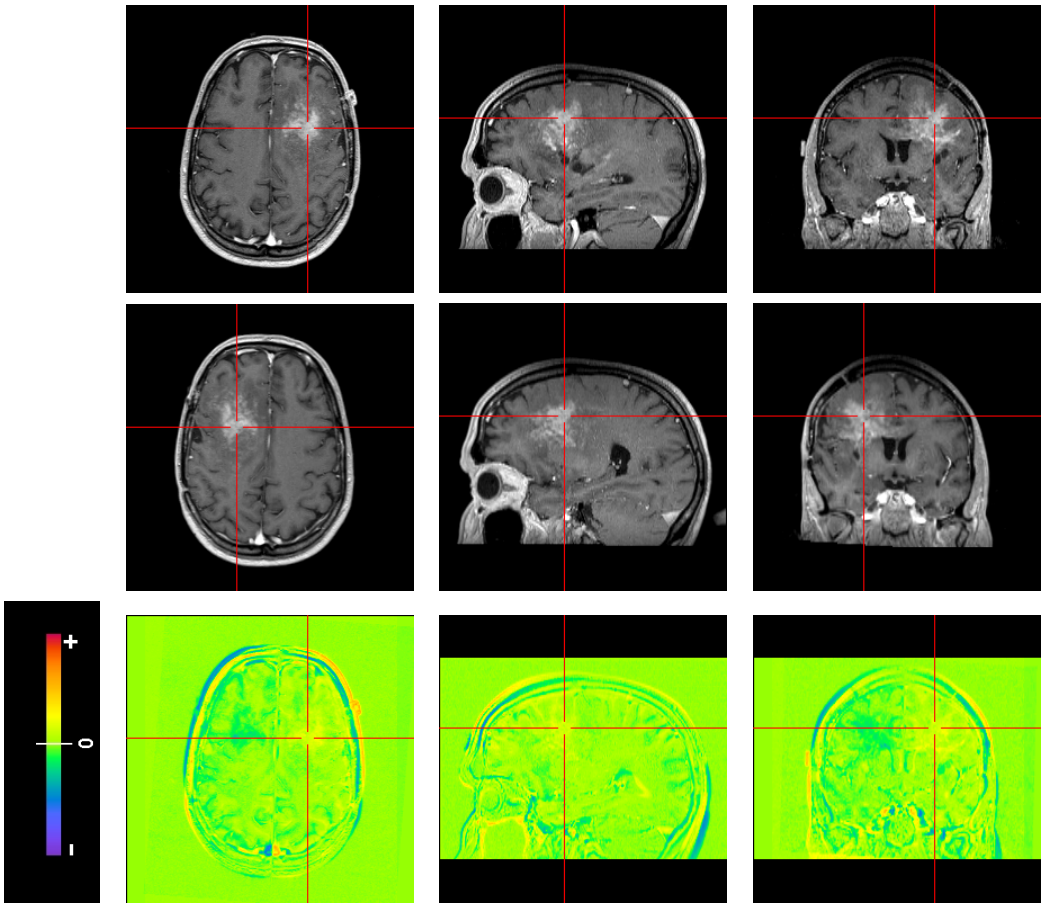

FIGURE 3.5. The top row of the figure shows the axial sagittal and the coronal views through an example patient image with a glioma in the right frontal lobe. The middle row shows the same views of the image reflected about the plane of symmetry. The bottom row shows the difference between the original and reflected images, where blue and violet represent negative values, yellow and red represent positive values, and green represents values near zero.

Figure 3.10 , that although global estimated displacement between the two groups, tumor subjects and controls, is roughly commensurate, the same can not be said of the global estimated additive intensity field. In the case of the tumor subjects, the global additive intensity field measure is roughly twice that found in the control subject group. This

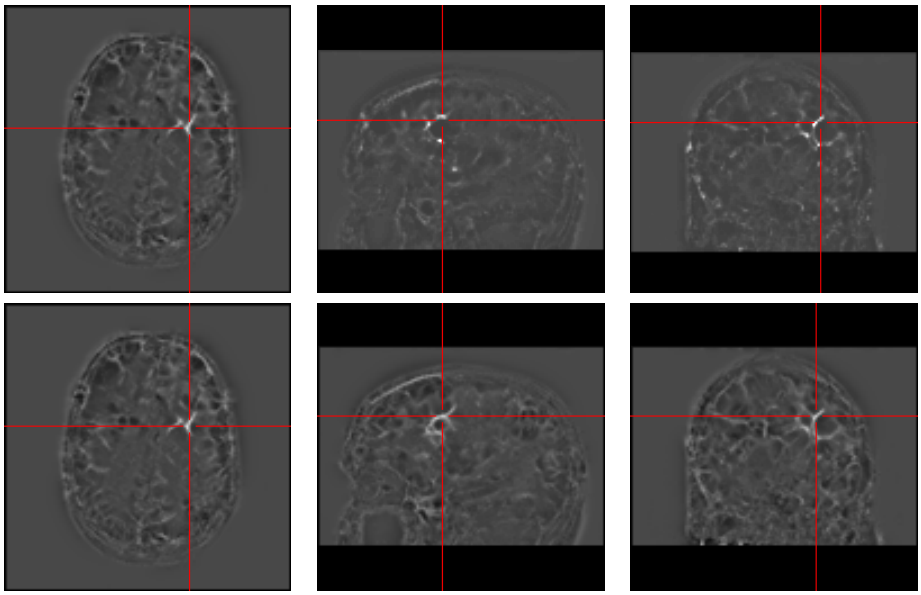

FIGURE 3.6. The top row shows the same views through the logarithm Jacobian of the transformation field $h(x)$. The bottom row shows the Divergence of the same.

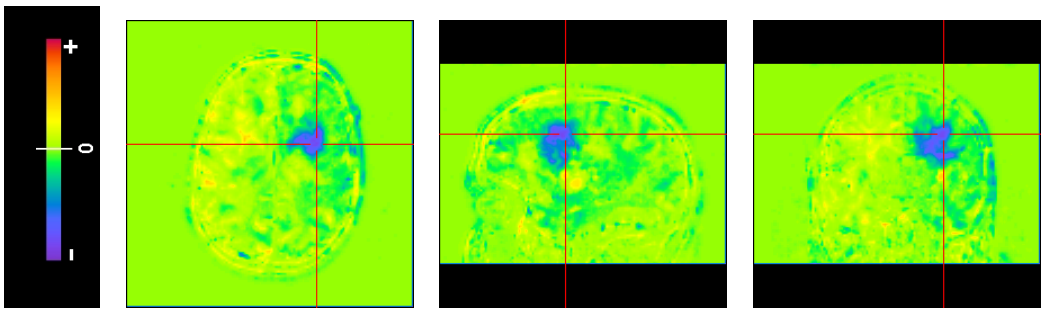

FIGURE 3.7. This row shows the same views through the estimated intensity field $f(x)$ capturing the inter-hemispheric radiometric differences.

is expected as the high dimensional warping is expected to accommodate normal bilateral asymmetry whereas the additive intensity field is expected to account for the gross asymmetry due to the presence of pathology.

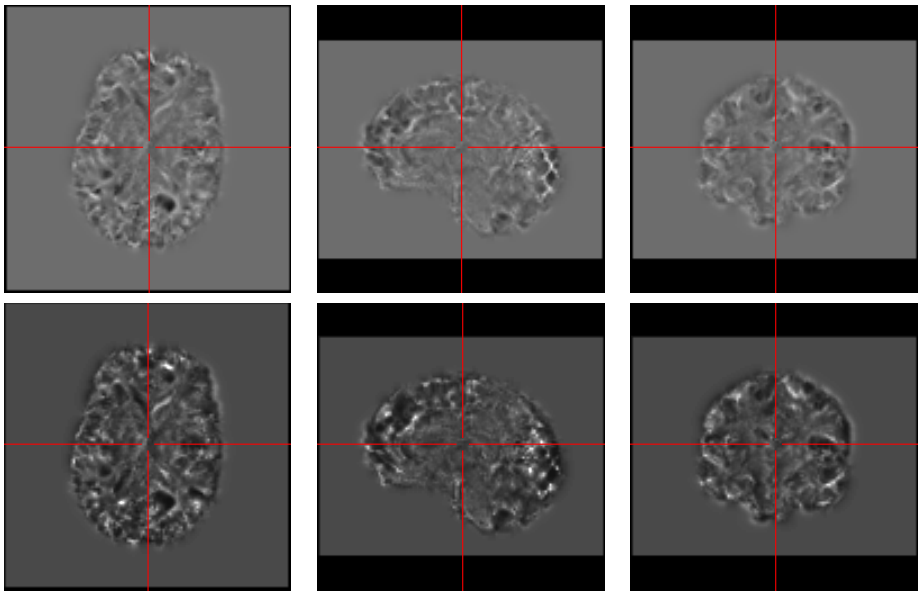

FIGURE 3.8. The top row shows the same views through the logarithm Jacobian of the transformation field $h(x)$. The bottom row shows the divergence of the same.

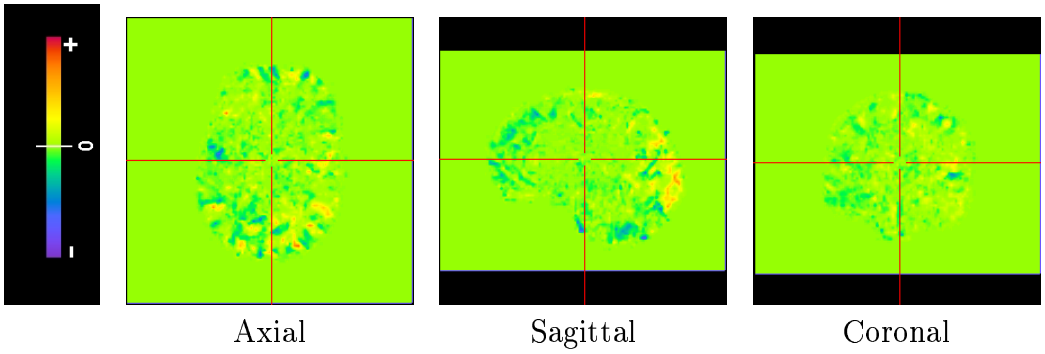

FIGURE 3.9. This row shows the same views through the estimated intensity field $f(x)$ capturing the inter-hemispheric radiometric differences.

These results provide only a rough qualitative difference between the tumor and normal controls and that robust statistical inference should not be drawn from them. A proper study would require that images taken from both groups be of the same resolution and controlled for patient characteristics such as age and gender.

TABLE 6. Per-voxel Average Normal Control Regularization Norms

Brain Volume (cm^3)	$\frac{1}{N}\int_\Omega ||L_d d(x)||^2 dx$	$\frac{1}{N}\int_\Omega ||L_f f_{\text{final}}(x)||^2 dx$
1,335.0	2.011e-03	5.50e+03
1,395.3	1.016e-03	6.96e+03
1,344.3	2.087e-03	1.05e+04
1,680.6	1.634e-03	6.49e+03

$d(x)$ is measured in voxel space
$f(x)$ is measured in intensity units
N is the number of voxels in the brain volume

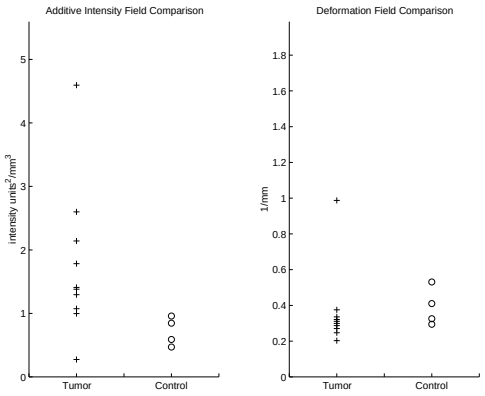

FIGURE 3.10. Tumor/Normal Comparison
Plot of Table 3 and Table 4 which compare the average per-voxel additive intensity field norms, $\frac{1}{N}\int_\Omega ||d(x)||^2 dx$, on the left and compare the average per-voxel deformation field norm, $\frac{1}{N}\int_\Omega ||f_{\text{final}}(x)||^2 dx$, on the right.

4. CONCLUSION

This paper presents a novel framework for analyzing structural and radiometric asymmetry in brain images. During the registration process radiometric intensity variation is accommodated via an additive intensity field. Since our framework is modality independent we would like to examine the asymmetry present in images of other modalities. This work will be used as part of a larger framework to automatically extract and analyze brain tumors.

As mentioned in Section 3 all the images presented in the paper are T1-weighted MR images without contrast agent. The addition of contrast agent would only affect the computed diffeomorphism if the

resulting increase in radiometric response (image intensity) was not symmetric with respect to the plane of symmetry.

5. Acknowledgments

The authors would like to thank Dr. Stephen Aylward of the department of radiology for his insightful suggestions and help during the development of this manuscript. We would also like to thank Nathan Moon for allowing us to use his image conversion utilities and Amy Chin Lorenzen for her assistance in editing the manuscript. The work was supported by NIH-NCI Grant R01 CA67812.

References

[1] L. Wang, S. C. Joshi, M. I. Miller, J. G. Csernansky, Statistical analysis of hippocampal asymmetry in schizophrenia, in press, NeuroImage .

[2] J. G. Csernansky, S. C. Joshi, L. Wang, J. P. Miller, M. I. Miller, Hippocampal morphometry in schizophrenia by high dimensional brain mapping, Proceedings of the National Academy of Science 95 (1998) 11406–11411.

[3] M. Styner, G. Gerig, Hybrid boundary-medial shape description for biologically variable shapes, in: Proc. of IEEE Workshop on Mathematical Methods in Biomedical Image Analysis (MMBIA) 2000, 2000, pp. 235–242.

[4] M. Styner, G. Gerig, Medial models incorporating object variability for 3d shape analysis, in: Information Processing in Medical Imaging, Springer, 2001, pp. 502–516.

[5] R. E. Hogan, K. E. Mark, L. Wang, S. C. Joshi, M. I. Miller, R. D. Bucholz, Mr imaging deformation-based segmentation of the hippocampus in patients with mesial temporal sclerosis and temporal lobe epilepsy, Epilepsia 40(Supl 7) (1999) 192.

[6] R. E. Hogan, K. E. Mark, L. Wang, S. Joshi, M. I. Miller, R. D. Bucholz, Mr imaging deformation-based segmentation of the hippocampus in patients with mesial temporal sclerosis and temporal lobe epilepsy, Radiology 216 (2000) 291–297.

[7] R. E. Hogan, R. D. Bucholz, I. Choudhuri, K. E. Mark, C. S. Butler, S. Joshi, Shape-analysis of hippocampal surface structure in patients with unilateral mesial temporal sclerosis, Journal of Digital Imaging 13 (2) (2000) 39–42.

[8] J. G. Csernansky, L. Wang, S. Joshi, J. Miller, M. Gado, D. Kido, D. McKeel, J. C. Morris, M. I. Miller, Early dat is distinguished from aging by high-dimensional mapping of the hippocampus, Neurology 55 (2000) 1636–1643.

[9] J. Thirion, S. Prima, G. Subsol, Statistical analysis of dissymmetry in volumetric medical images, IEEE Workshop on Biomedical Image Analysis (1998) 74–83.

[10] S. Prima, J. Thirion, G. Subsol, N. Roberts, Automatic analysis of normal dissymmetry of males and females in mr images, Proceedings of Medical Image Computing and Computer-Assisted Intervention (1998) 770–779.

[11] C. Sun, J. Sherrah, 3d symmetry detection using the extended gaussian image, IEEE Transactions on Pattern Analysis and Machine Intelligence 19 (2).

[12] J. Moossy, G. S. Zubenko, A. J. Martinez, G. R. Rao, Bilateral symmetry of morphologic lesions in alzheimer's disease [see comments], Archives of Neurology 45 (3) (1988) 251–254.

[13] S. Smith, M. Jenkinson, Accurate robust symmetry estimation, Proceedings of Medical Image Computing and Computer-Assisted Intervention (1999) 308–317.

[14] P. M. Thompson, J. Moussai, S. Zohoori, A. Goldkorn, A. A. Khan, M. S. Mega, G. W. Small, J. L. Cummings, A. W. Toga, Cortical variability and asymmetry in normal aging and alzheimer's disease, Cerebral Cortex 8 (6) (1998) 492–509.

[15] P. M. Thompson, M. S. Mega, C. Vidal, J. L. Rapoport, A. W. Toga, Detecting disease-specific patterns of brain structure using cortical pattern matching and a population-based probabilistic brain atlas, in: Information Processing in Medical Imaging, Springer, 2001, pp. 488–501.

[16] P. Lorenzen, S. Joshi, G. Gerig, E. Bullitt, Tumor-induced structural and radiometric asymmetry in brain images, in: Proceedings of the Workshop on Mathematical Methods in Biomedical Image Analysis, 2001, pp. 163–170.

[17] G. Christensen, S. Joshi, M. Miller, Deformable templates using large deformation kniematics, IEEE Transactions on Medical Imaging 16 (1997) 864–877.

[18] G. Christensen, R. Rabbitt, M. Miller, 3d brain mapping using a deformable neuroanatomy, Physics in Medicine and Biology 39 (1994) 209–618.

[19] M. I. Miller, S. C. Joshi, G. E. Christensen, Large deformation fluid diffeomorphisms for landmark and image matching, in: A. W. Toga (Ed.), Brain Warping, Academic Press, 1999, pp. 115–131.

[20] J. Talairach, P. Tournoux, Co-Planar Stereotaxis Atlas of the Human Brain, Georg Thiem Verlag, 1988.

[21] Y. Liu, Robust midsagittal plane extraction from course, pathological 3d images, Proceedings of Medical Image Computing and Computer-Assisted Intervention .

[22] Y. Liu, R. T. Collins, W. E. Rothfus, Robust midsagittal plane extraction from normal and pathological 3-d neuroradiology images, IEEE Transactions on Medical Imaging 20 (3).

[23] B. A. Ardekani, J. Kershaw, M. Braun, I. Kanno, Automatic detection of the mid-sagittal plane in 3-d brain images, IEEE Transactions on Medical Imaging 16 (6).

[24] S. Prima, S. Ourselin, N. Ayache, Computation of the mid-sagittal plane in 3d medical images of the head, European Conference on Computer Vision .

[25] S. C. Joshi, M. I. Miller, G. E. Christensen, A. Banerjee, T. A. Coogan, U. Grenander, Hierarchical brain mapping via a generalized dirichlet solution for mapping brain manifolds, in: Proc. of the SPIE's 1995 International Symposium on Optical Science, Engineering, and Instrumentation, Vol. 2573, August, 1995, pp. 278–289.

[26] D. Luenberger, Optimization by Vector Space Methods, John Wiley and Sons, 1969.

[27] C. Davatzikos, Spatial transformation and registration of brain images using elastically deformable models, Comp. Vision and Image Understanding 66 (2) (1997) 207–222.

[28] J. C. Gee, R. K. Bajcsy, Elastic matching: Continuum mechanical and probabilistic analysis, in: A. W. Toga (Ed.), Brain Warping, Academic Press, 1999.
[29] A. W. Toga, Brain Warping, Academic Press, 1999.
[30] J.-P. Thirion, G. Calmon, Deformation analysis to detect and quantify active lesions in 3D medical image sequences, INRIA Technical Report 3101, 1997.
[31] E. Kreysig, Advanced Engineering Mathematics, John Wiley and Sons, 1983.